Supplemental information to:
The potential role of methanesulfonic acid (MSA) in aerosol formation and growth and the associated radiative forcings

Anna L. Hodshire[1], Pedro Campuzano-Jost[2,3], John K. Kodros[1], Betty Croft[4], Benjamin A. Nault[2,3], Jason C. Schroder[2,3], Jose L. Jimenez[2,3], Jeffrey R. Pierce[1]

[1]Department of Atmospheric Science, Colorado State University, Fort Collins, CO 80523, USA
[2]Department of Chemistry, University of Colorado, Boulder, CO, USA
[3]Cooperative Institute for Research in Environmental Sciences, University of Colorado, Boulder, CO, USA
[4]Dalhousie University, Department of Physics and Atmospheric Science, Halifax, NS, B3H 4R2, Canada

Correspondence to: Anna L. Hodshire (Anna.Hodshire@colostate.edu)

S1. Simulated ammonia concentrations

Annually (Fig. S1) and seasonally (Fig. S2) averaged simulated concentrations of ammonia from the GEOS-Chem-TOMAS model. Each map is made from the reported ammonia concentrations for the DEFAULT_NoMSA model.
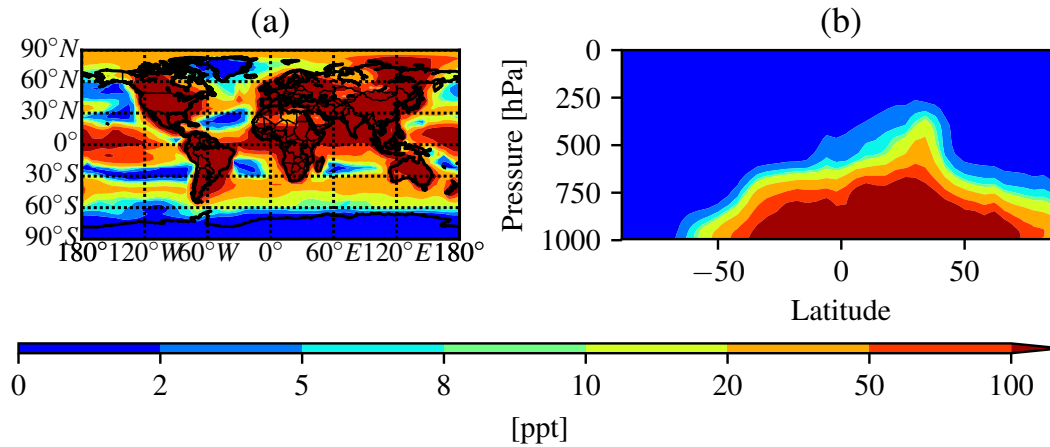
Figure S1. Global annual average predicted NH_3 concentrations at (a) the surface and (b) zonally. For the PARAM_NoNuc and PARAM_Nuc cases, it's assumed that if $[NH_3] <$ 10 ppt (blue colors), then the model is under low-base (no free ammonia) conditions (Figure 1a).
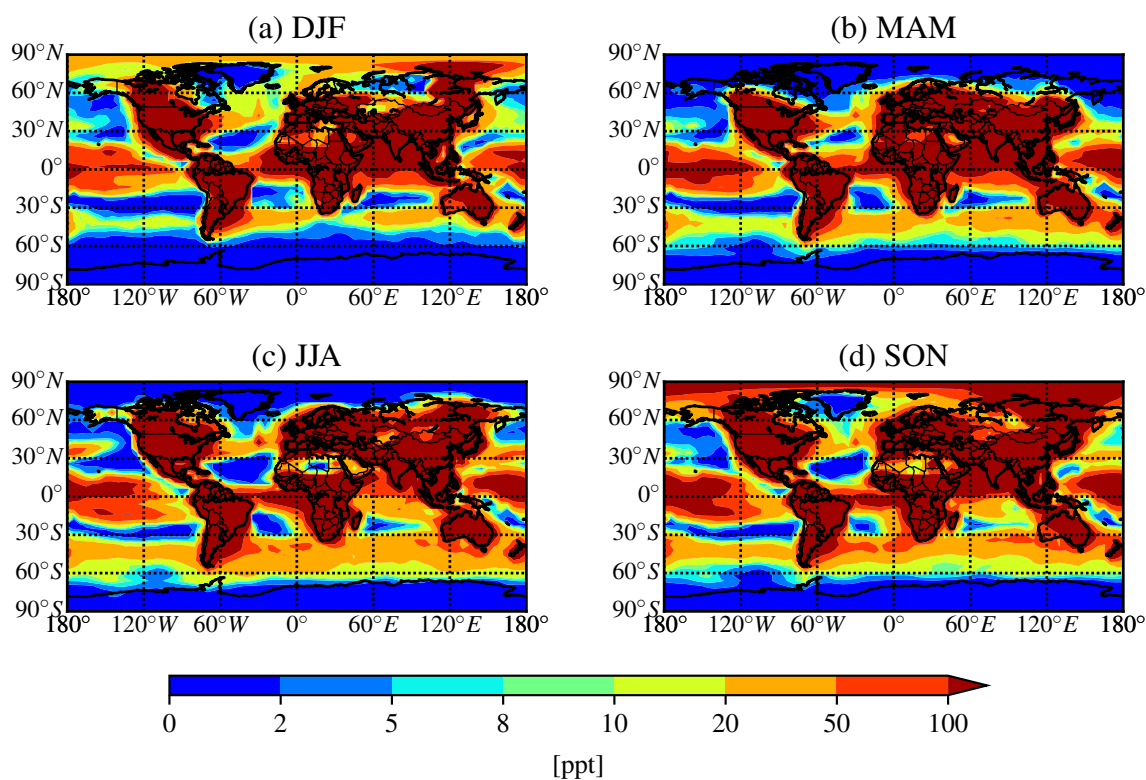
Figure S2. Global seasonal average predicted NH$_3$ concentrations at the surface for: (a) December, January, February; (b) March, April, May; (c) June, July, August; and (d) September, October, November. For the PARAM_NoNuc and PARAM_Nuc cases, it's assumed that if [NH$_3$] < 10 ppt (blue colors), then the model is under low-base (no free ammonia) conditions (Figure 1a).

S2. Comparison of different DMS emission inventories in GEOS-Chem-TOMAS.

We test the sensitivity of the size distribution towards the DMS emissions in two ways: (1) we replace the default DMS emissions inventory for GEOS-Chem v10.01 (Kettle et al., 1999; Kettle and Andreae, 2000) with the updated emissions inventory by Lana et al., (2010) and (2) we increase the default DMS emissions inventory globally by a factor of two. We hereon refer to each inventory as the default DMS inventory, the Lana DMS inventory, and the 2xDMS inventory. The results of these tests are shown in Tables S1-S2 and Figs. S3-S5. Table S1 and Fig. S3 shows the comparisons between each DEFAULT_NoMSA simulation (DEFAULT_NoMSA, DEFAULT_NoMSA_Lana, and DEFAULT_NoMSA_2xDMS) and the NoDMS simulation. This indicates the contribution from sulfate and sulfuric acid produced by DMS/SO$_2$ oxidation for each DMS emissions inventory. Table S2 and Fig. S4-S5 shows the comparisons between each PARAM_NoNuc case and each DEFAULT_NoMSA case for submicron aerosol mass (only in Table S2), N3 and N80 (Fig. S5) and the AIE and DRE (Fig. S6). It is seen that for the Lana DMS inventory, both the NoDMS (Fig. S3) and PARAM_NoNuc_Lana (Figs. S4-S5) case comparisons have only small spatial differences and similar magnitude of effects as compared to the default DMS inventory. Thus, if DMS emissions are better simulated by the Lana DMS inventory, our general conclusions would not be changed about the effects of MSA towards the size distribution.

The 2xDMS inventory shows some non-trivial changes in N80 for some regions and levels as compared to the default DMS inventory for the NoDMS comparison (Table S1; Fig. S3), primarily with increases in N80 over the Antarctic between 800-500 hPa and over ~20°S -20° N between 500-100 hPa, and decreases in N80 over 50°-90° N between 1000-750 hPa. The increase in sulfuric acid from DMS/SO$_2$ oxidation will boost particle formation and growth rates in relatively clean regions, such as the Antarctic. There will also be a boost from condensed sulfate from aqueous oxidation of DMS, further increasing the sizes but not necessarily number concentration of larger particles. However, the PARAM_NoNuc_2xDMS case is very similar to the PARAM_NoNuc case (Table S2; Figs. S4 and S5) and again, we conclude that even if DMS emissions are globally increased by up to a factor of two, our general conclusions would not be changed about the effects of MSA towards the size distribution.

Table S1. Annual mean % changes at 900 hPa for the contribution of the sulfate and sulfuric acid from DMS/SO₂ oxidation for submicron aerosol mass, N3, N80, and radiative forcing changes in AIE and DRE for each DEFAULT_NoMSA emissions inventory. Positive values of a metric indicate that the sulfate and sulfuric acid increases that metric compared to a simulation with no DMS emissions.

Case	Submicron aerosol mass global (30-90 S) % change	N3 global (30-90 S) % change	N80 global (30-90 S) % change	AIE global (30-90 S) change in mW m^{-2}	DRE global (30-90 S) change in mW m^{-2}
DEFAULT_NoMSA - NoDMS_NoMSA	5.0 % (7.3 %)	7.3 % (19.5 %)	12.2 % (24.3 %)	-46 (-38)	-120 (-170)
DEFAULT_NoMSA_Lana - NoDMS	5.0 % (7.6 %)	7.0 % (19.4 %)	12.6 % (24.8 %)	-51 (-39)	-130 (-200)
DEFAULT_NoMSA_2xDMS - NoDMS	8.0 % (12.6 %)	7.5 % (22.9 %)	16.3% (35.4 %)	-92 (-130)	-220 (-330)

Table S2. Annual mean % changes at 900 hPa for the MSA for submicron aerosol mass, N3, N80, and radiative forcing changes in AIE and DRE for the PARAM_NoNuc simulations using each DEFAULT_NoMSA emissions inventory. Positive values of a metric indicate that MSA increases that metric compared to the DEFAULT_NoMSA case per emissions inventory.

Case	Submicron aerosol mass global (30-90 S) % change	N3 global (30-90 S) % change	N80 global (30-90 S) % change	AIE global (30-90 S) change in mW m^{-2}	DRE global (30-90 S) change in mW m^{-2}
PARAM_NoNuc - DEFAULT_NoMSA	0.7 % (1.3 %)	-3.9 % (-8.5 %)	0.8 % (1.7 %)	-8.6 (-17)	-15 (-26)
PARAM_NoNuc_Lana - DEFAULT_NoMSA_Lana	0.7 % (1.3%)	-3.5 % (-7.1 %)	0.8 % (1.7 %)	-7.8 (-14)	-16 (-28)
PARAM_NoNuc_2xDMS - DEFAULT_NoMSA_2xDMS	1.2 % (2.3 %)	-4.3 % (-7.7 %)	0.3 % (0.6 %)	-6 (-3.1)	-28 (-46)
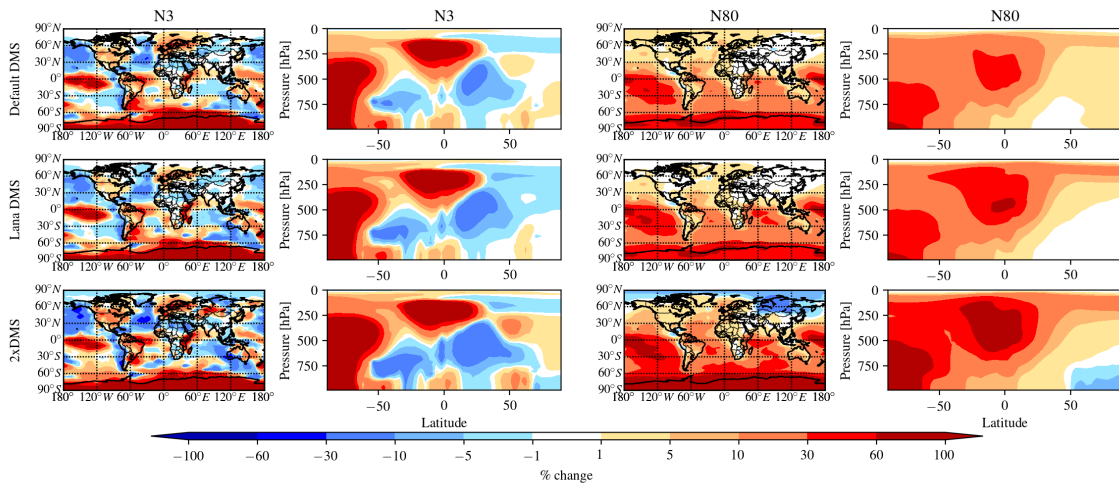
Figure S3. Global annual mean percent change at 900 hPa (first and third column) and global zonal annual mean percent change (second and fourth column) between NoDMS_NoMSA and the DEFAULT_NoMSA case (first row), the DEFAULT_NoMSA_Lana case (second row), and the DEFAULT_NoMSA_2xDMS case (third row). First and second column: N3 (the number concentration of particles with diameters larger than 3 nm). Third and fourth column: N80. Warm colors indicate that the inclusion of DMS/SO₂ oxidation products in the model increases N3/N80.
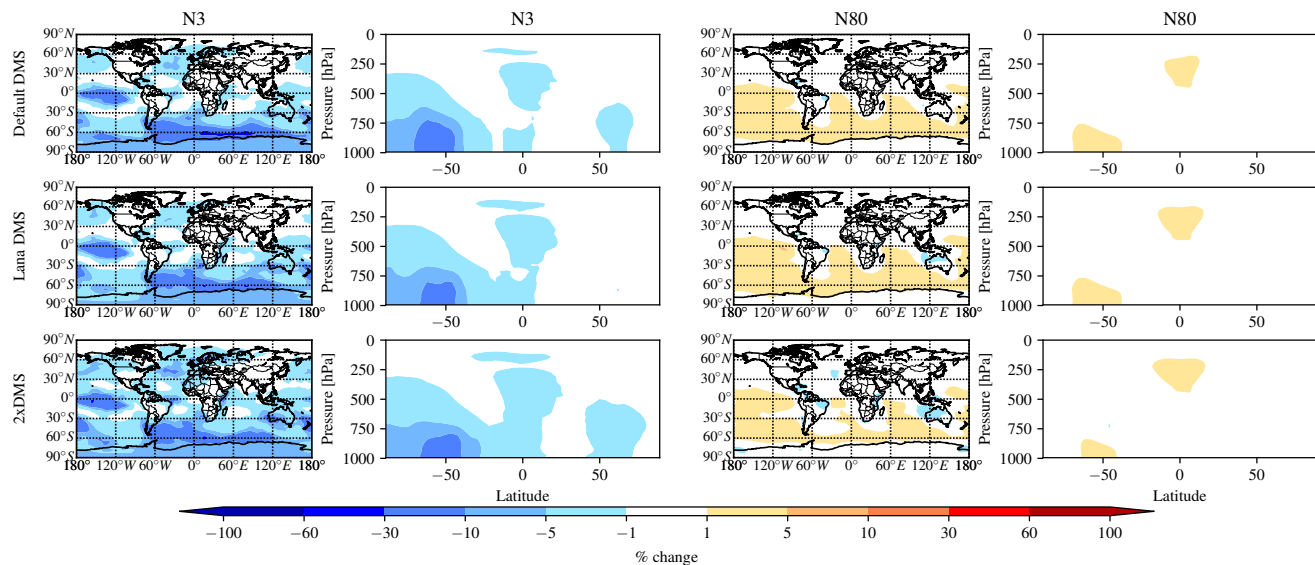
Figure S4. Global annual mean percent change at 900 hPa (first and third column) and global zonal annual mean percent change (second and fourth column) between the DEFAULT_NoMSA case and PARAM_NoNuc case (first row), the DEFAULT_NoMSA_Lana case and PARAM_NoNuc_Lana case (second row), and the DEFAULT_NoMSA_2xDMS case and PARAM_NoNuc_2xDMS case (third row). First and second column: N3 (the number concentration of particles with diameters larger than 3 nm). Third and fourth column: N80.
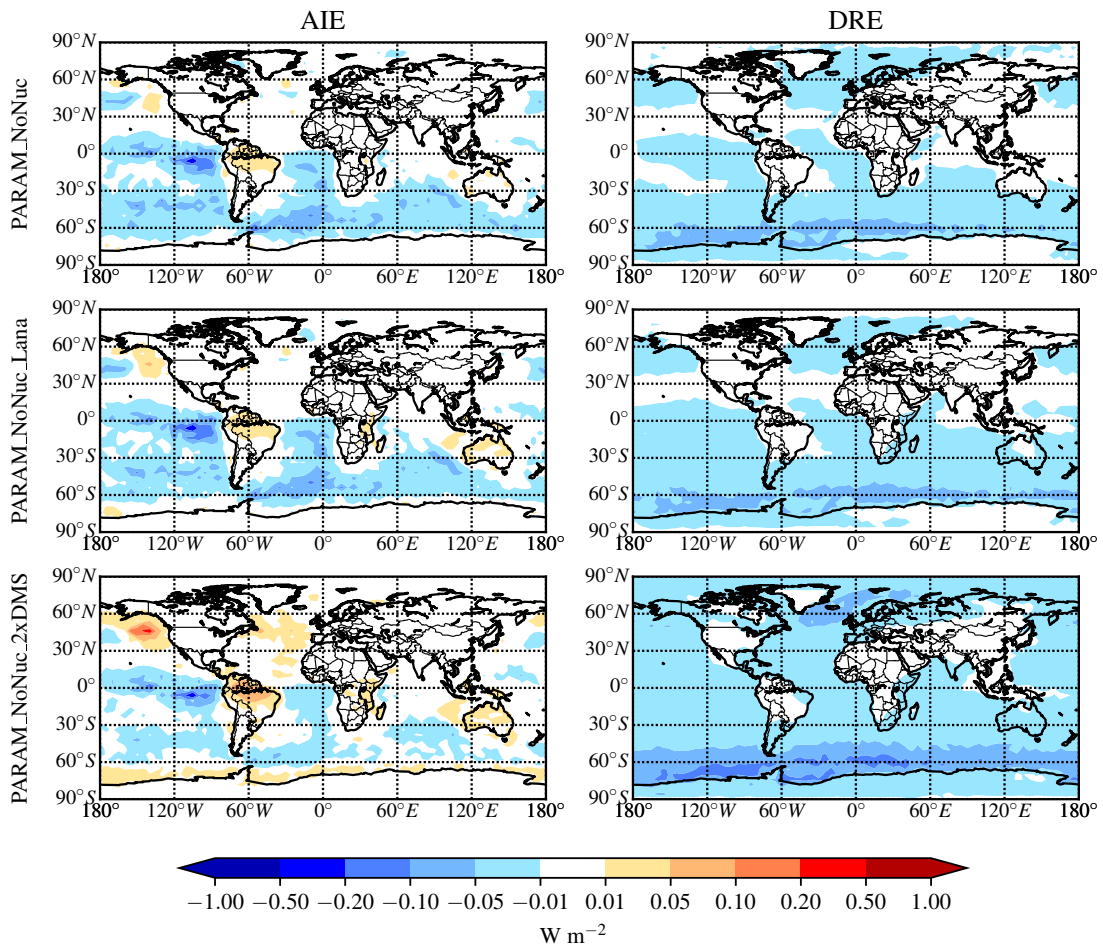
Figure S5. Global annual mean percent change for the AIE (first column) and DRE (second column) between the DEFAULT_NoMSA case and PARAM_NoNuc case (first row), the DEFAULT_NoMSA_Lana case and PARAM_NoNuc_Lana case (second row), and the DEFAULT_NoMSA_2xDMS case and PARAM_NoNuc_2xDMS case (third row).

S3. Global annual mean number concentrations for the DEFAULT_NoMSA case; additional results

      Figure S6 provides the number concentrations (N3 and N80) at 900 hPa and zonally for the base case (DEFAULT_NoMSA). Table S3 provides the quantitative values for Fig. 6 (main text).
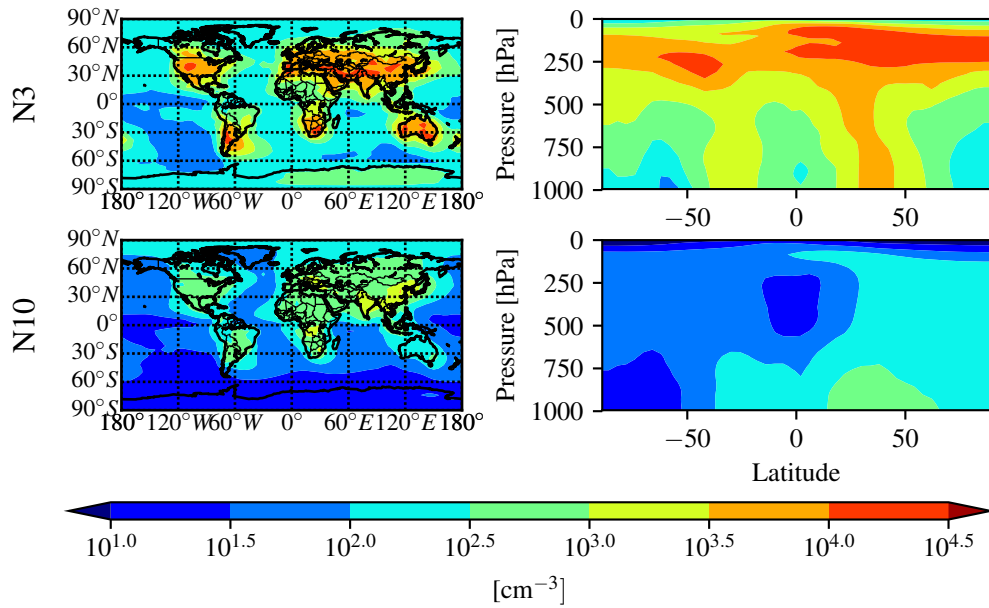
Figure S6. The number concentration (cm⁻³) normalized to STP for the BASE case. Top row: N3 at cloud level (900 hPa; right) and zonally (left). Bottom row: N80 for cloud level (900 hPa; right) and zonally (left).

Table S3. Annual mean % changes due to MSA at 900 hPa for each MSA simulation relative to the DEFAULT_NoMSA simulation for submicron aerosol mass, N3, N80, and radiative forcing changes in AIE and DRE. Positive values for any metric for PARAM_NoNuc, ELVOC_NoNuc, SVOC_NoNuc, PARAM_Nuc, and ELVOC_Nuc all indicate that the addition of MSA increases that metric relative to the DEFAULT_NoMSA simulation. The DEFAULT_NoMSA-NoDMS_NoMSA row shows the contribution of the sulfate and sulfuric acid from DMS/SO$_2$ oxidation present in the DEFAULT_NoMSA simulation; positive values of a metric indicate that the sulfate and sulfuric acid increases that metric compared to a simulation with no DMS emissions.

Case	Submicron aerosol mass global (30-90 S) % change	N3 global (30-90 S) % change	N80 global (30-90 S) % change	AIE global (30-90 S) change in mW m^{-2}	DRE global (30-90 S) change in mW m^{-2}
PARAM_NoNuc - DEFAULT_NoMSA	0.7 % (1.3 %)	-3.9 % (-8.5 %)	0.8 % (1.7 %)	-8.6 (-17)	-15 (-26.0)
ELVOC_NoNuc - DEFAULT_NoMSA	1.2 % (2.5%)	-8.9 % (-20.8 %)	9.1 % (22.2 %)	-75 (-150)	-20 (-34)
SVOC_NoNuc - DEFAULT_NoMSA	1.2 % (2.5 %)	-6.0 % (-12.6 %)	-0.2 % (-0.12 %)	7.5 (11)	-25 (-44)
PARAM_Nuc - DEFAULT_NoMSA	0.7 % (1.3 %)	112.5 % (309.9 %)	2.1 % (4.4 %)	-26 (-48)	-14 (-24)
ELVOC_Nuc - DEFAULT_NoMSA	1.2% (2.6%)	153.4 % (397.7 %)	23.8 % (56.3 %)	-180 (-390)	-13 (-20)
DEFAULT_NoMSA - NoDMS_NoMSA (indicates contribution from DMS/SO$_2$ oxidation)	5.0 % (7.3 %)	7.3 % (19.5 %)	12.2 % (24.3 %)	-46 (-38)	-120 (-170)

S4. ATom-1 and ATom-2 plots

The ATom-1 and ATom-2 campaigns took place during July 28-August 22, 2016, and January 26-February 22, 2017, respectively. Both campaigns took measurements from the Pacific and Atlantic Basin. Figures S7-S10 provide the 1:1 plots for each separate campaign and each separate ocean basin for the main MSA sensitivity cases in this study, PARAM_NoNuc, ELVOC_NoNuc, SVOC_NoNuc, PARAM_Nuc, and ELVOC_Nuc. Also shown are the 5:1 and 1:5 lines. Each subplot indicates the log mean bias (LMB), slope (m), and coefficient of determination (R^2) for each sensitivity case as compared to the measurements. Figures S11-S14 show the zonally averaged simulated MSA concentrations for each model level for each basin and campaign with the corresponding particle-phase MSA measurements overlaid. (The up and down patterns represent the flight tracks of the NASA DC-8 aircraft.)
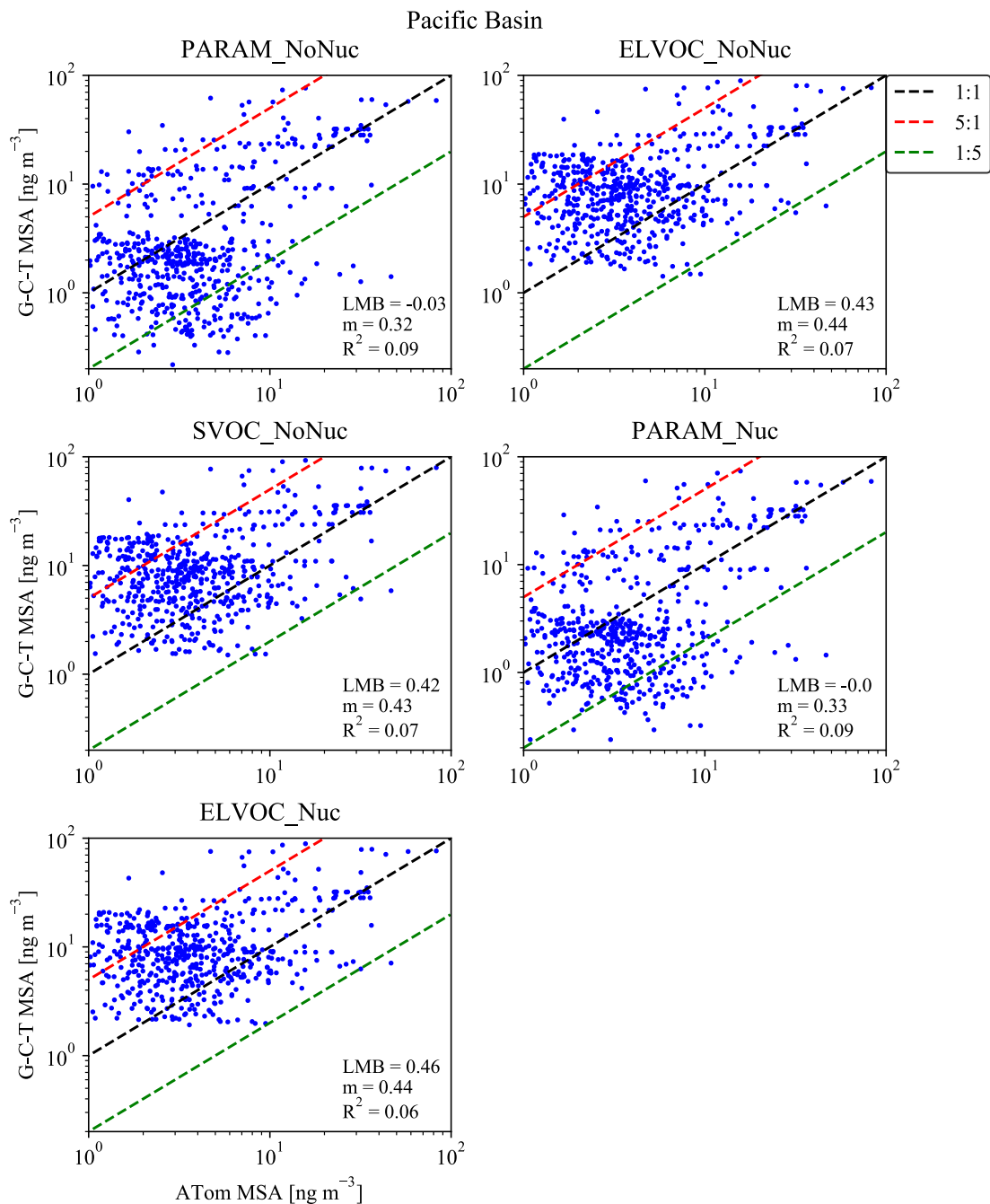
Figure S7. 1:1 (black dashed line) plots for the simulated mean MSA mass for the month of August and measured MSA mass during the ATom-1 campaign (July 28-August 22 2016) for the Pacific basin flight tracks, calculated log-mean bias (LMB), slope (*m*), and coefficient of determination (R^2). The red and green dashed lines indicate 5:1 and 1:5 lines. Simulated MSA mass is calculated by subtracting the total sulfate mass for the base case from each sensitivity case.
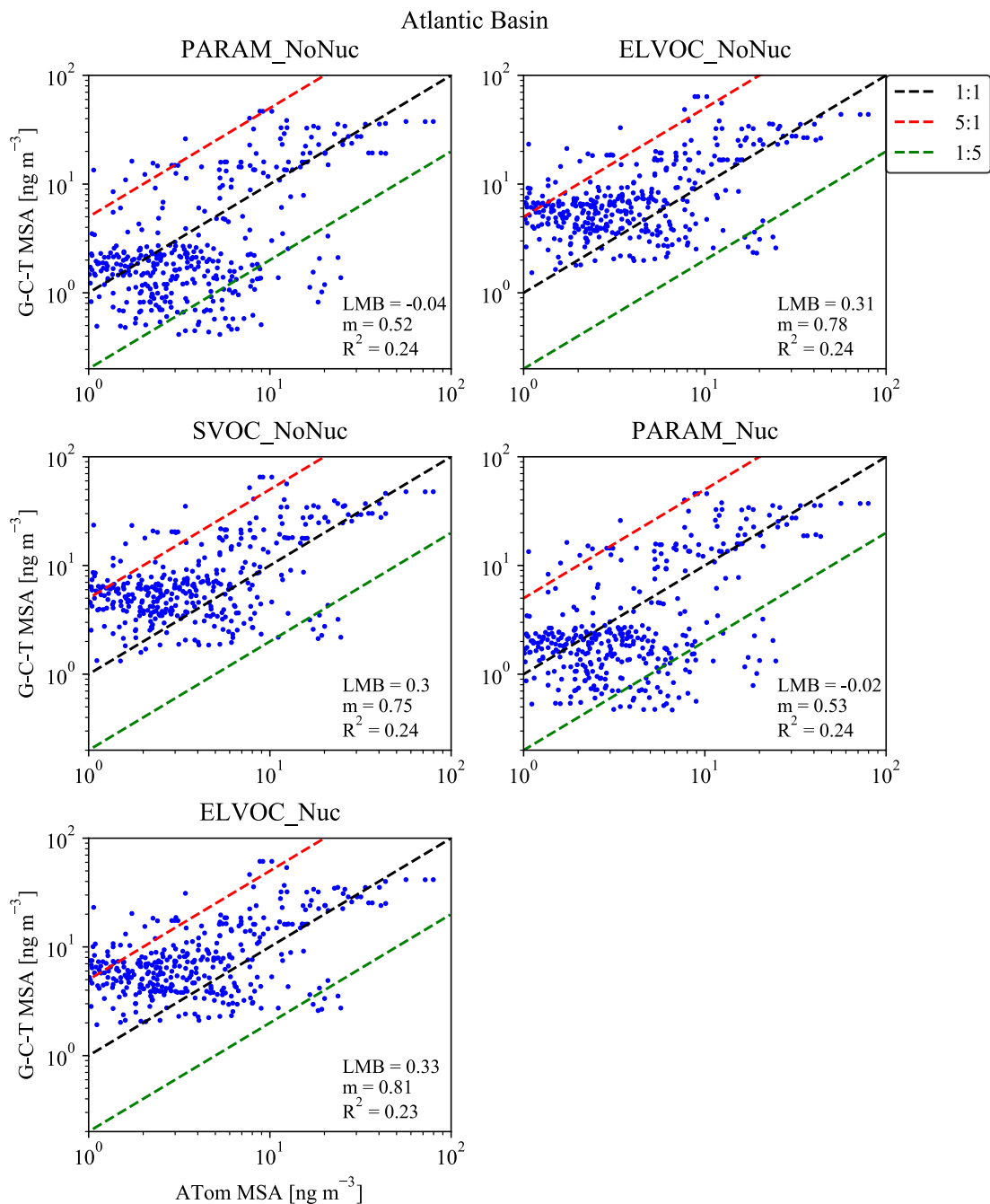
Figure S8. 1:1 (black dashed line) plots for the simulated mean MSA mass for the month of August and measured MSA mass during the ATom-1 campaign (July 28-August 22 2016) for the Atlantic basin flight tracks, calculated log-mean bias (LMB), slope (m), and coefficient of determination (R^2). The red and green dashed lines indicate 5:1 and 1:5 lines. Simulated MSA mass is calculated by subtracting the total sulfate mass for the base case from each sensitivity case.
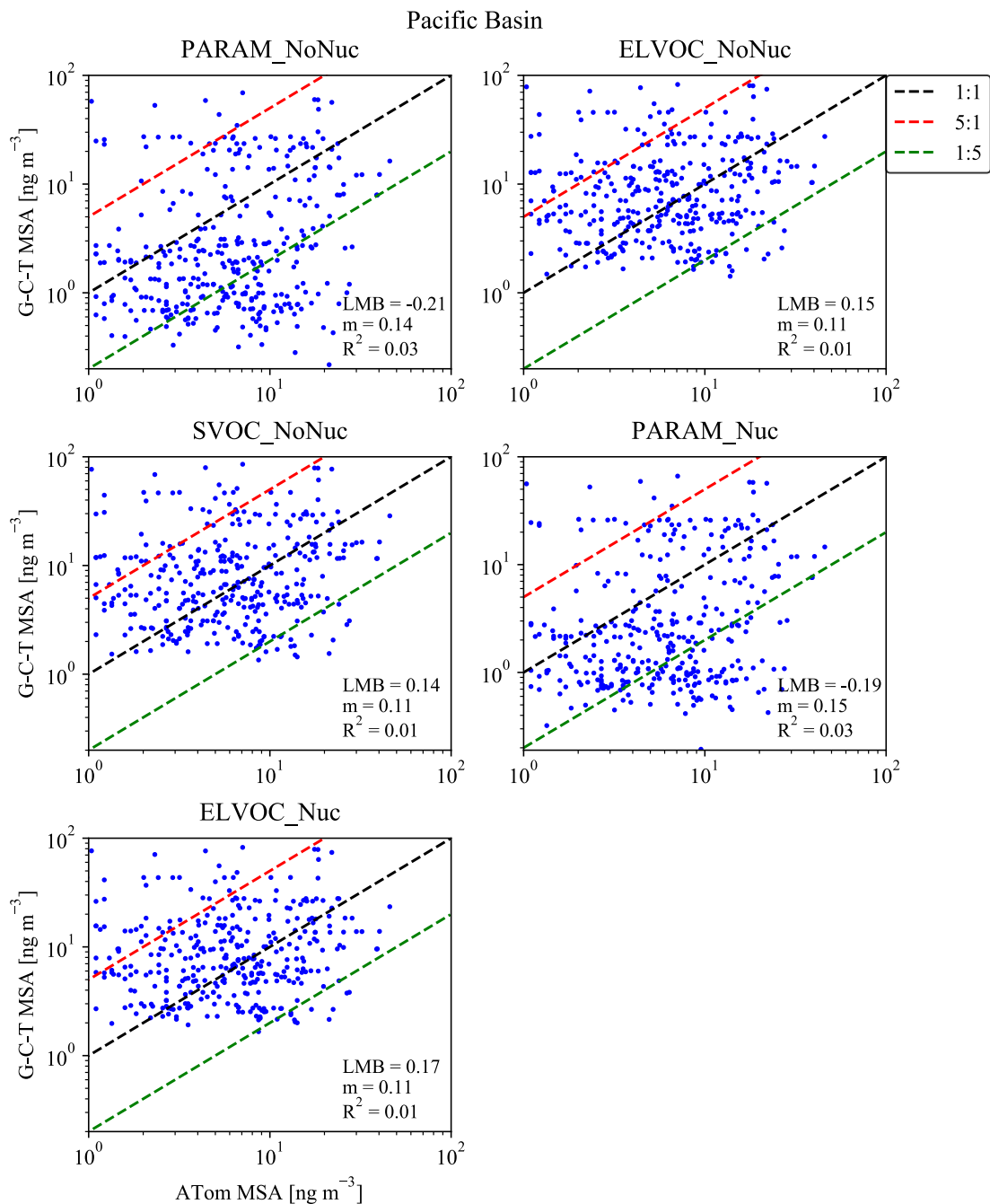
Figure S9. 1:1 (black dashed line) plots for the simulated mean MSA mass for the month of February and measured MSA mass during the ATom-2 campaign (January 26-February 22 2017) for the Pacific basin flight tracks, calculated log-mean bias (LMB), slope (*m*), and coefficient of determination (R^2). The red and green dashed lines indicate 5:1 and 1:5 lines. Simulated MSA mass is calculated by subtracting the total sulfate mass for the base case from each sensitivity case.
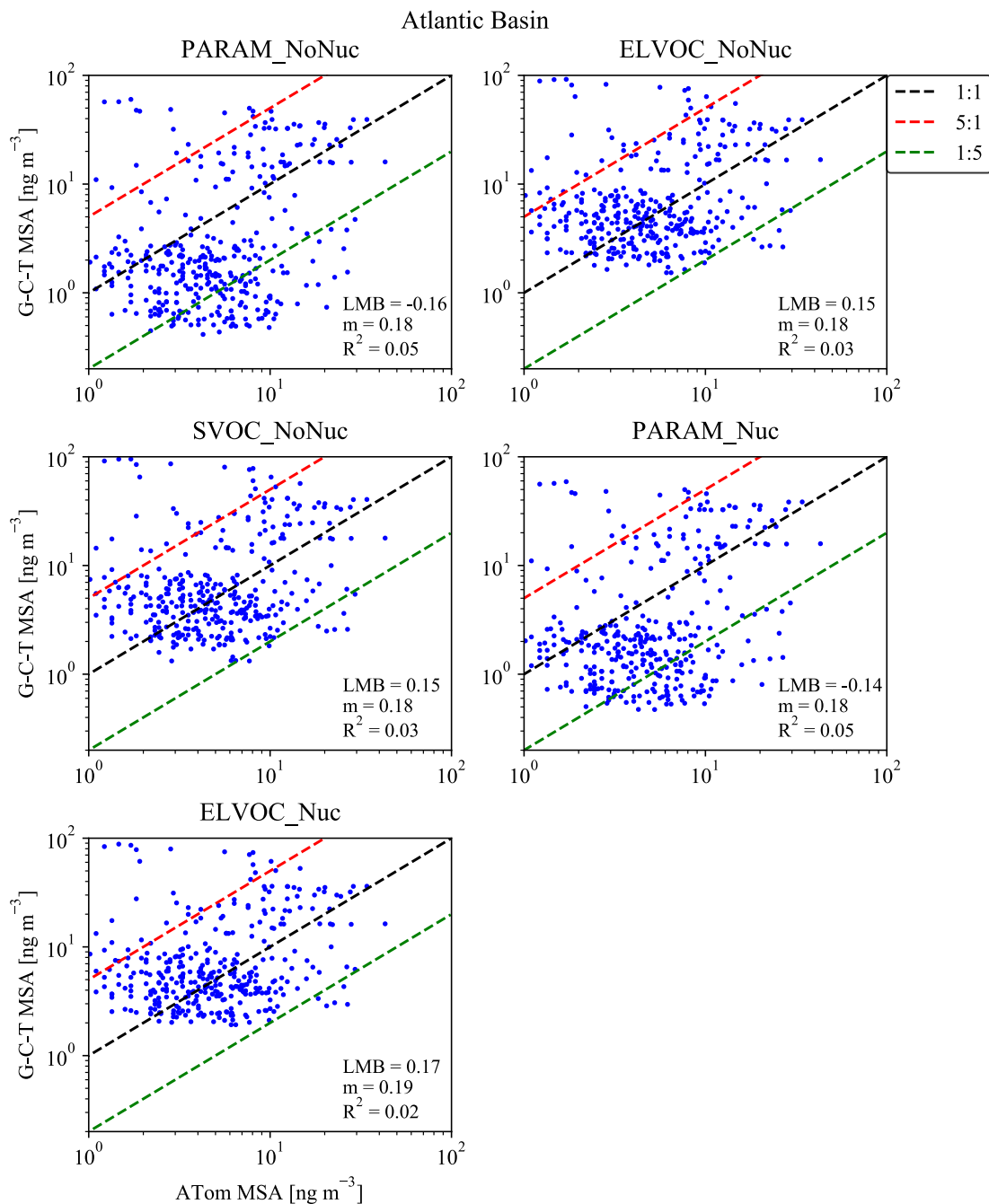
Figure S10. 1:1 (black dashed line) plots for the simulated mean MSA mass for the month of February and measured MSA mass during the ATom-2 campaign (January 26-February 22 2017) for the Atlantic basin flight tracks, calculated log-mean bias (LMB), slope (m), and coefficient of determination (R^2). The red and green dashed lines indicate 5:1 and 1:5 lines. Simulated MSA mass is calculated by subtracting the total sulfate mass for the base case from each sensitivity case.
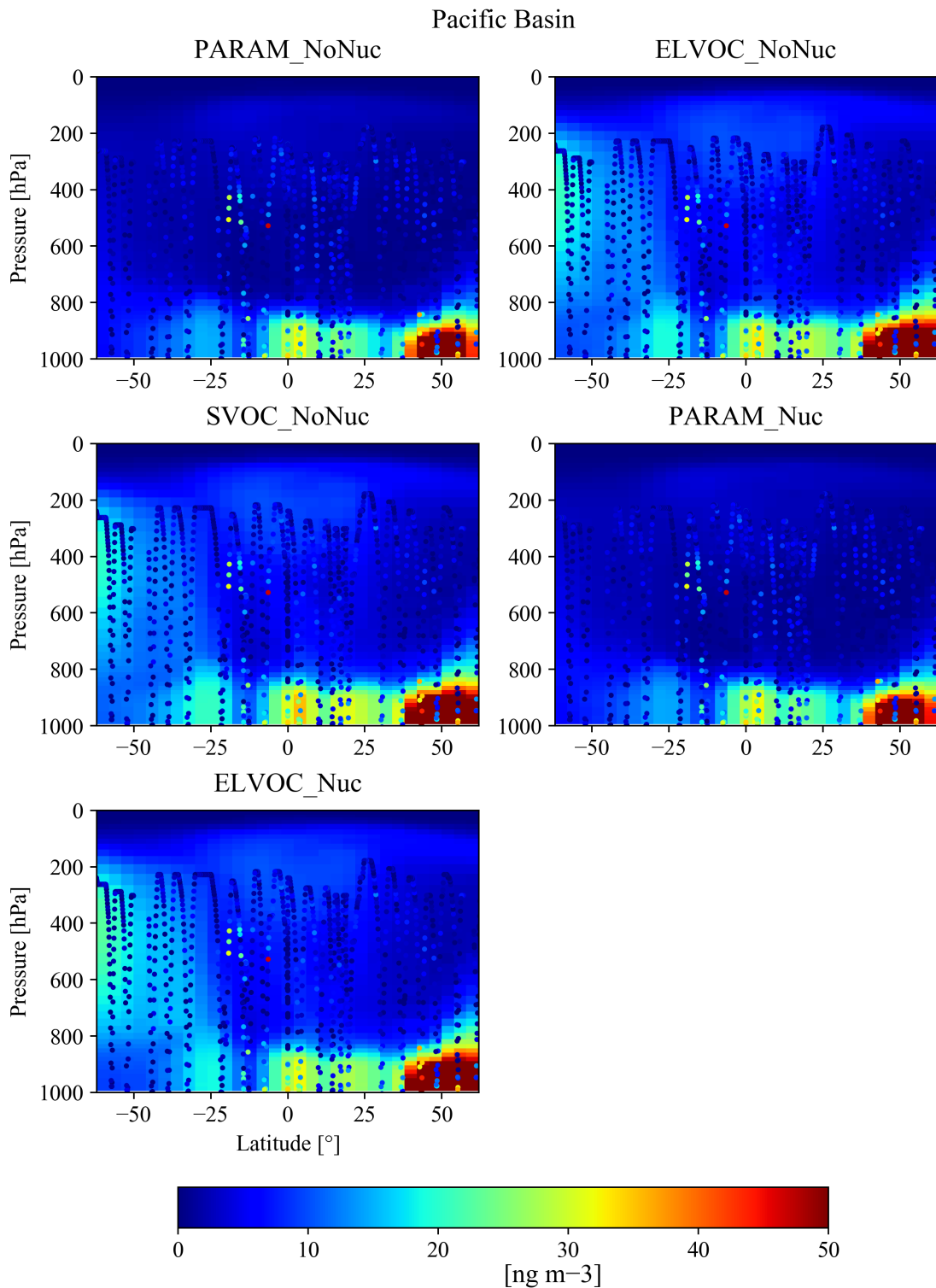
Figure S11. Comparison of simulated mean MSA mass for the month of August to measured MSA mass (circles) during the ATom-1 campaign (July 28-August 22 2016) for the Pacific basin flight tracks. Simulated MSA mass is calculated by subtracting the total sulfate mass for the base case from each sensitivity case.
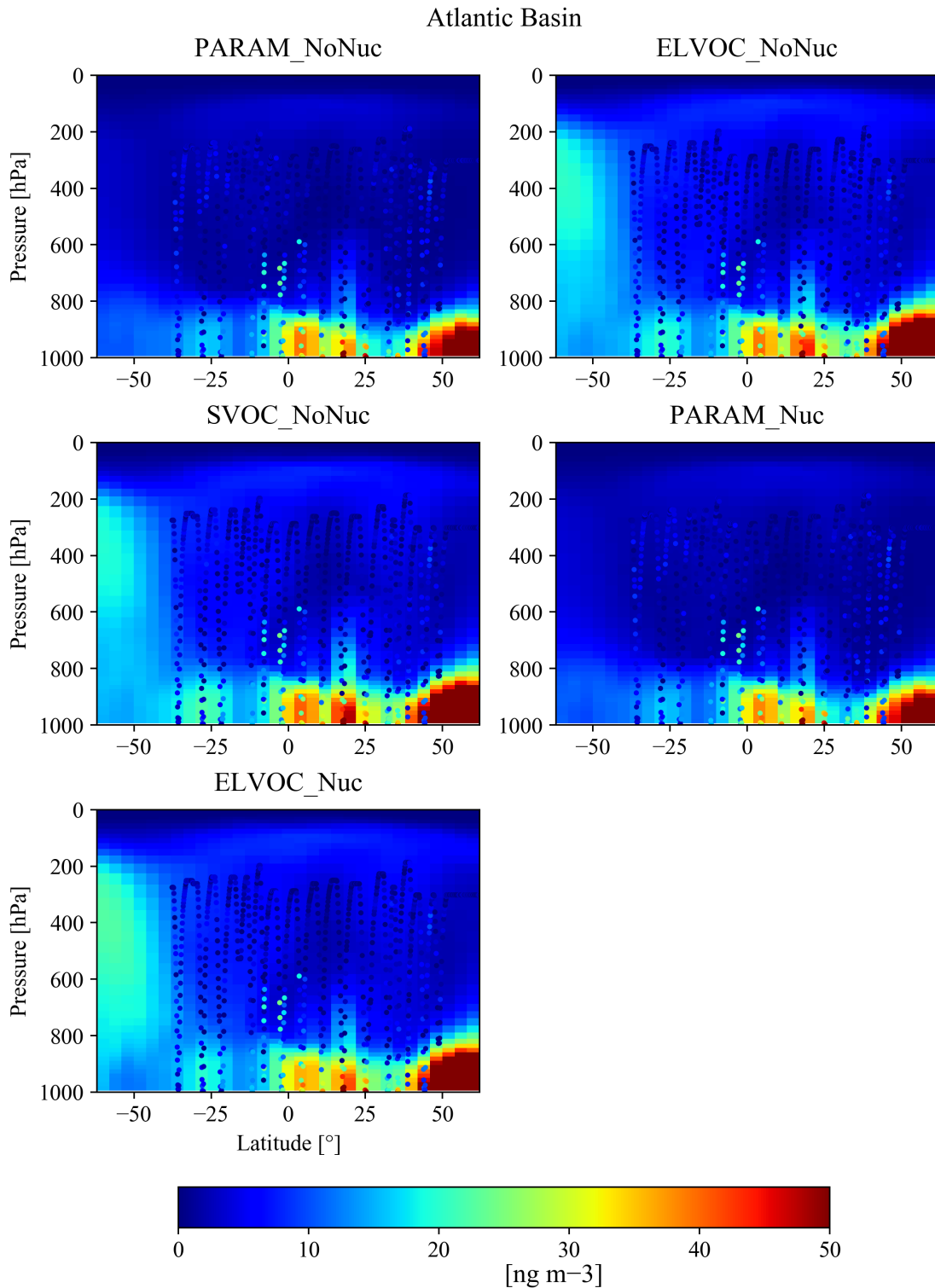
Figure S12. Comparison of simulated mean MSA mass for the month of August to measured MSA mass (circles) during the ATom-1 campaign (July 28-August 22 2016) for the Atlantic basin flight tracks. Simulated MSA mass is calculated by subtracting the total sulfate mass for the base case from each sensitivity case.
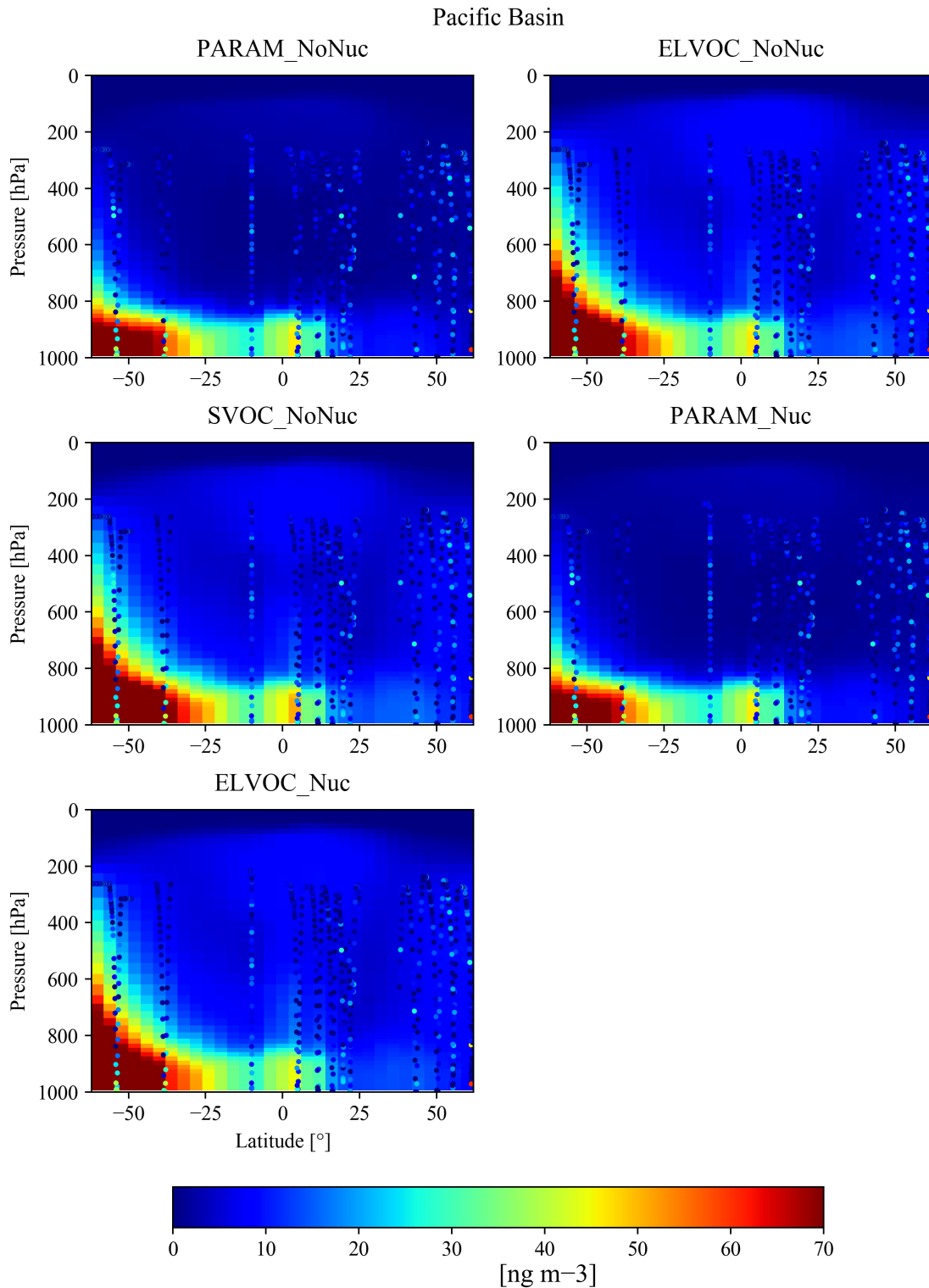
Figure S13. Comparison of simulated mean MSA mass for the month of February to measured MSA mass (circles) during the ATom-2 campaign (January 26-February 22 2017) for the Pacific basin flight tracks. Simulated MSA mass is calculated by subtracting the total sulfate mass for the base case from each sensitivity case.
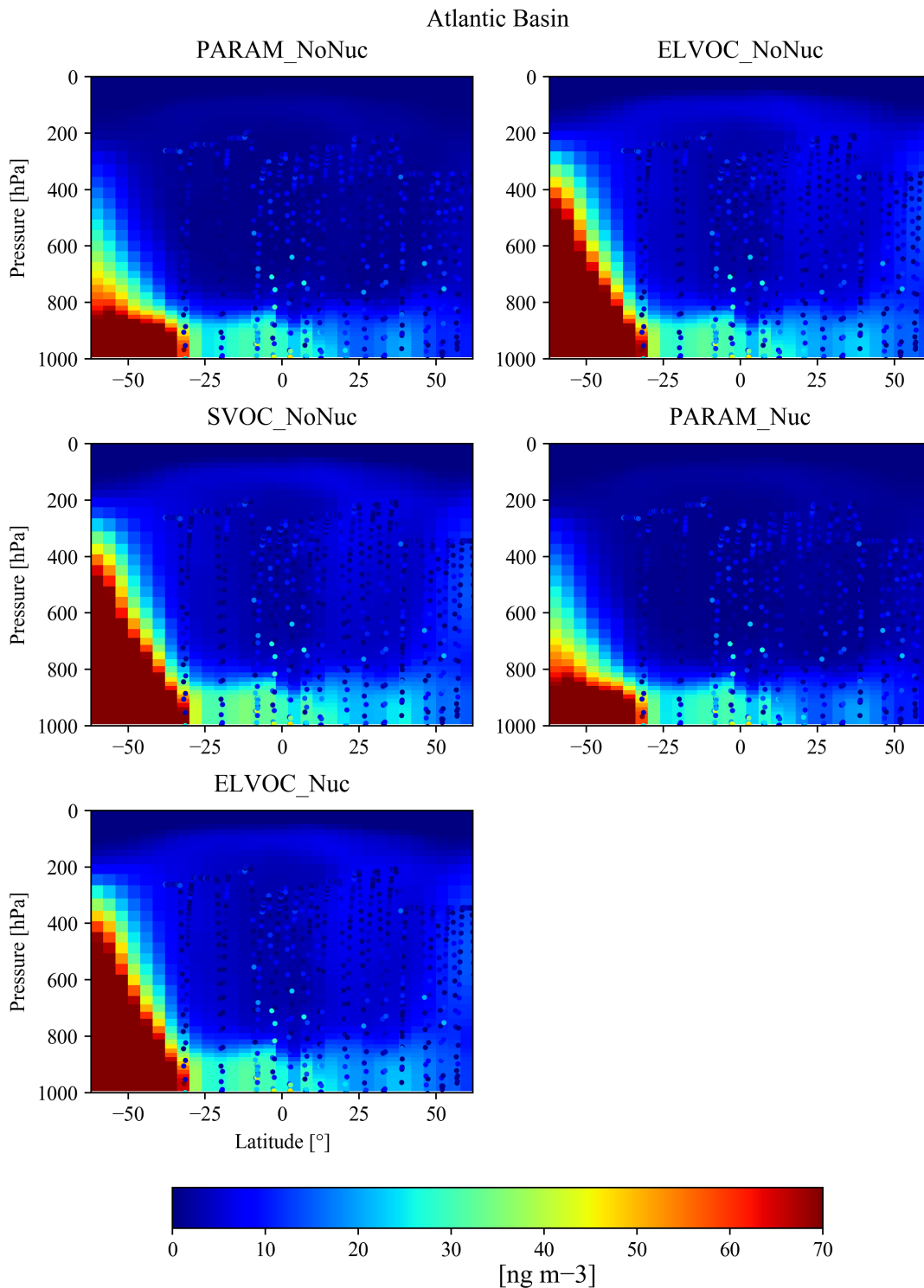
Figure S14. Comparison of simulated mean MSA mass for the month of February to measured MSA mass (circles) during the ATom-2 campaign (January 26-February 22 2017) for the Atlantic basin flight tracks. Simulated MSA mass is calculated by subtracting the total sulfate mass for the base case from each sensitivity case.

S5. MSA Calibration Details for the Aerosol Mass Spectrometer

S5.1. General Approach

As shown first by Phinney et al. (2006), $CH_3SO_2^+$ is a highly specific ion for the identification of MSA in AMS spectra. A number of groups have since used this ion as a calibrated marker for quantification of MSA. Other quantification approaches have also been used but they have often have proven less robust as discussed in Huang et al. (2017).

This quantification procedure requires the determination of two MSA specific quantities (Zorn et al., 2008, Huang et al., 2015, Willis et al., 2016, Huang et al., 2017):
- The ratio of the $CH_3SO_2^+$ ion to the total AMS signal from MSA, $f(CH_3SO_2)$, and
- The relative ionization efficiency of the total AMS response (ion current) from MSA relative to nitrate (the primary AMS calibrant), RIE_{MSA}. Once those quantities are known, the MSA concentration can be determined as follows (based on the general expression for calculating species concentrations in the AMS; Canagaratna et al., 2007):

$$[MSA] = \frac{C}{CE} \frac{MW_{MSA}}{IE_{MSA}} \sum I_{MSA} = \frac{C}{CE} \frac{MW_{NO3}}{RIE_{MSA} IE_{NO3}} \frac{I_{CH3SO2}}{f(CH_3SO_2)} \quad (Eq.\,S1)$$

In this equation I_{CH3SO2} refers to the signal of the marker ion (in ion counts, our measured variable), IE_{NO3} is the ionization efficiency of the instrument for nitrate, CE is the collection efficiency, MW_{MSA} and MW_{NO3} are the molar masses of MSA and nitrate, respectively, and C is a proportionality constant that includes the MS duty cycle, flow calibration, and unit conversions.

Both of these quantities were determined over a series of both laboratory and in-field calibrations (starting at the end of the ATom-1 deployment) by atomizing either pure dilute MSA solutions (Aldrich, >99.9% purity), or dilute solutions that were previously neutralized with excess aqueous ammonia (Aldrich, ACS reagent). The nebulizer output for the neutralized solutions (effectively $NH_4CH_3SO_3$, referred to as AMSA in the following) was size-selected with an SMPS (TSI 3936) and the aerosol number concentration was recorded with a collocated CPC (TSI 3010). Due to the high amounts of ammonium (from the daily ammonium nitrate calibrations) present in our in-field calibration system, the nebulized pure MSA aerosol was introduced directly into the AMS to avoid neutralization in the SMPS. Hence, for acidic MSA, only the fragmentation pattern was investigated.

S5.2. Estimation of minor ion contributions

In order to account properly for the total ion signal of MSA, the contribution of some ions that had a high background was estimated by indirect means:
- The contribution of both water ions ($O_2 HO^+$, and H_2O^+, "familyHO" in AMS parlance) and CO_2^+ were obtained from unconstrained linear regressions, so they could be separated from the gas phase contributions. Since the AMS flying on ATom uses a cryopump for background reduction, the water background is low enough for this method to work (typically $H_2O:N_2 \sim 0.1$ for the background signals).

-        The contribution of the sulfur ion (S^+) to the AMS signal was estimated based on the abundance of the (independently fitted) $^{34}S^+$ isotope at low MSA concentrations, and fitted directly at high concentrations (> 1 mg sm^{-3})

-        The contribution of CO^+ to the AMS signal was estimated from fitting $C^{18}O^+$, but was found to be negligible at all times (<1%)

Figure S15a shows a typical regression of the different ion species for an AMSA calibration, while Fig. S15b shows the contributions of the water, sulfur and CO_2^+ ions to the total signal for all calibrations. On average, the contribution of these ions to the total MSA signal are small (about 5% in total), in contrast to sulfate (discussed in S5.5).
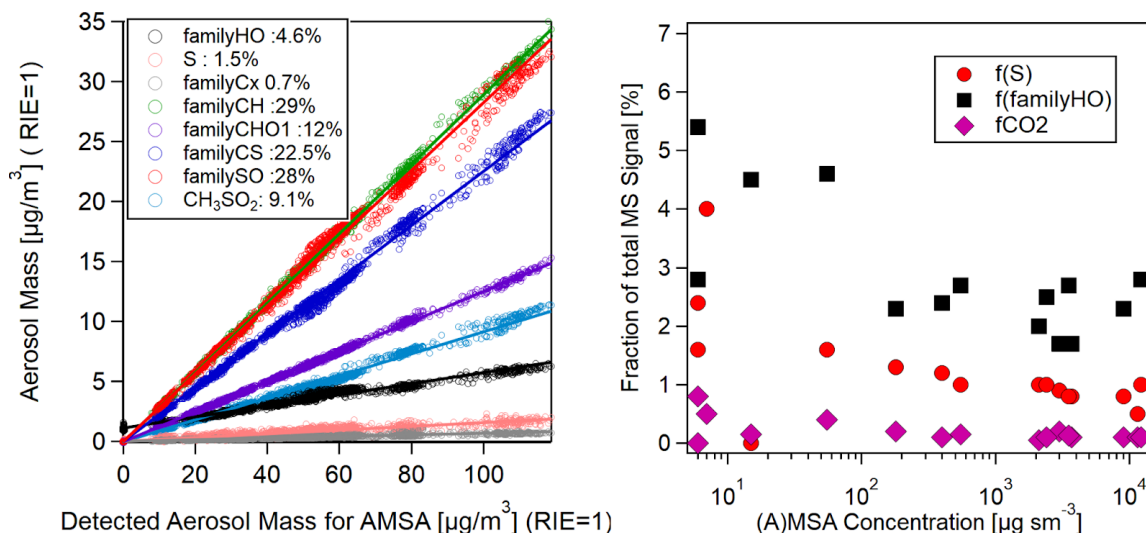
Figure S15. (left) Determination of the fractional ion contributions (summed up into chemical families) in the AMS (including water, sulfur and CO_2) of MSA for an AMSA calibration at intermediate concentrations ([MSA]~10-50 µg sm^{-3}, as determined by SMPS measurements). (right) Contributions of S^+, CO_2^+ and water ions to the total AMS signal of MSA for all the ATom calibrations (calibrations were done with both AMSA and MSA, but only MSA was quantified).

S5.3. Quantification of the Relative Ionization Efficiency of MSA (RIE$_{MSA}$)
        RIE$_{MSA}$ was derived from two different approaches:
1. Relative to the ammonium *RIE (RIE$_{NH4}$)* after back-to-back calibrations with ammonium nitrate ("ammonium balance method") analogous to the most-commonly used method for the determination of sulfate and chloride *RIE* (Schroder et al., 2018). This assumes that, as in the case of sulfate, the analyzed particles are fully neutralized when introduced into the AMS. In the case of another ammonium salt of an organic acid, ammonium oxalate, some studies have suggested partial evaporation of ammonia prior to analysis (Jimenez et al., 2016). Thermodynamic calculations suggest that this is due to the H(COOH)$_2^+$ being a weak acid (pK$_a$=4.19, Lide 2008), leading to some formation of molecular oxalic acid and subsequent partitioning of NH$_3$ to the gas phase, but not of oxalic acid given its much lower vapor pressure. Given that MSA is a strong acid (pKa=-1.96 (Guthrie, 1978)), this is not expected for AMSA, and in fact no difference in

these experiments was observed when the AMSA solution was saturated with NH$_4$OH (vs just neutralized). This method is independent of AMS transmission, collection efficiency and possible evaporation of the semivolatile AMSA prior to AMS sampling.

2. Determining the value of of RIE_{MSA} that is needed for the AMS to match the aerosol mass calculated from simultaneous measurements by the SMPS/CPC ("mass closure method") (Willis et al., 2016; Huang et al., 2017). This requires generating a monodisperse aerosol with little to no doubly charged particles and knowledge of both the density and collection efficiency of AMSA. In addition, for a semivolatile species such as MSA (p_{vap}=6*10^{-4} Torr at 20° C, Tang and Munkelwitz, 1991) there could be differences due to potential evaporation in the CPC and AMS lines, which would complicate the comparison. Both monodispersity and effective density (which was sometimes lower than the bulk density of 1.48 g cm^{-3}, Lide et al., 2008) were confirmed with particle time-of-flight measurements (PToF, de Carlo et al, 2004). Single particle measurements (described in detail below) confirmed that CE was close to 1 and that evaporation was a minor concern. Therefore a CE of 1 was used. Assuming negligible evaporation/wall deposition in the lines both methods should yield similar results.

Figure S16 shows data for 2 AMSA calibrations at low concentrations taken one year apart where the RIE_{MSA} for both methods agreed within 5% and the corresponding PToF measurements. We hence report RIE_{MSA} = 1.70 ± 0.08 based on the more accurate ammonium balance method, while using the difference with the mass closure method as a conservative uncertainty estimate. This RIE_{MSA} was used for the all four ATom deployments, given the small change (<5%) in the other RIEs of the instrument over these campaigns.
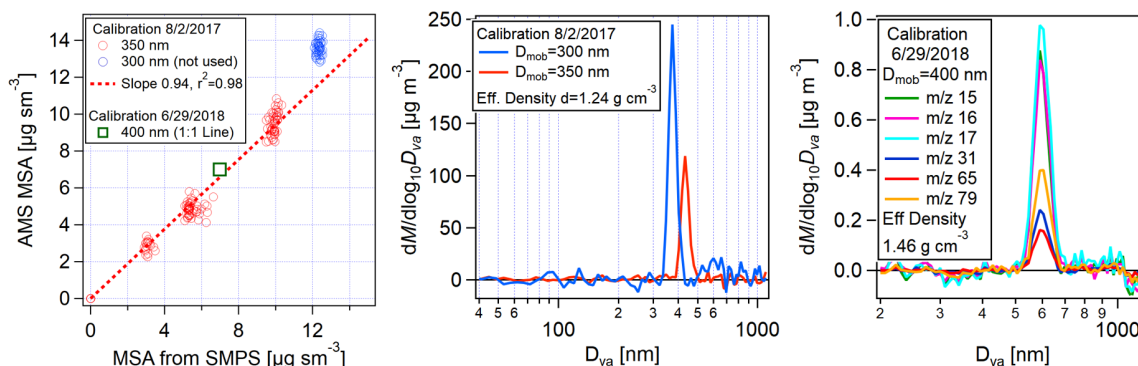
Figure S16. (left) Regression of the AMS response for MSA with the calculated SPMS mass of the test aerosol for two different calibrations of the CU AMS instrument using NH$_4$SO$_3$CH$_3$ (AMSA) taken one year apart. AMS response was calculated using f(CH$_3$SO$_2$) from the calibration and an RIE_{MSA} derived from the ion balance (1.7 on 8/2/2017, 1.72 on 6/29/2018); the SPMS mass was calculated using the density determined from the D$_{va}$/D$_{geo}$ ratio for each calibration (DeCarlo et al., 2004). (middle) Particle time-of-flight size distribution of the test aerosol for the 8/2/2017 calibration, used to determine the density and confirm monodispersity. (right) AMS PToF-mode size

distribution for the 6/29/2018 calibration, showing the same m/z ions that were used in the analysis of the single particle experiments (Figure S19).

S5.4. Robustness of the MSA Mass Spectral Pattern in the AMS

Zorn et al. (2008) reported that the fragmentation pattern of MSA was highly dependent on vaporizer temperature. Special care was taken during ATom to keep the vaporizer temperature constant at ~600°C by keeping the vaporizer current constant and periodically calibrating the instrument response with $NaNO_3$ (Hu et al., 2017). The MSA fragmentation pattern at low concentrations (comparable and larger than ambient concentrations) was observed to be very stable over the course of the four ATom deployments.

However, significant changes in $f(CH_3SO_2)$ were observed when higher calibration particle concentrations were used (Figure S17a). Figure S17b shows the variability in time of the main ion families that contribute to the MSA signal for a typical AMSA calibration at higher concentrations. While NH_4 shows an very fast and stable response, for MSA a fraction of the signal shows a slower time response after each background cycle (which some ion groups showing this trend stronger than others; this will be discussed in more detail in Section S5.7). The rate of equilibration is concentration dependent, hence at higher concentrations not only do the relative ion ratios change, but also the overall signal recorded by the AMS, resulting in larger apparent values of RIE_{MSA} at higher concentrations. This effect only appears to be important at very high concentrations of 100s to 1000s of µg m^{-3}, but we document it here since calibrations are often performed at such higher concentrations. Based on these results, we recommend calibrating at concentrations similar to ambient levels.

It is important to note that the magnitude of this effect is very dependent on the acquisition cycle of the AMS: For the CU-AMS, which operates in "fast mode" (6 s closed, 46 s open, Schroder et al., 2018), the time available for MSA reaching some of sort of equilibrium in the ionizer is substantially longer than in the standard AMS acquisition sequence (4 s closed, 6 s open). Hence RIE_{MSA} taken at similar concentrations in the standard AMS acquisition mode may be lower than the values that we reported above. However, it is also possible that the slower response if more important in the CU AMS instrument, as the presence of a cryopump surface cooled to 90 K around the ionizer region will lower the equilibrium temperature of the ionizer, compared to standard AMS instruments. Since at least some of the slow response may be due to particles or gases deposited on the ionizer surfaces, this lower temperature could play a role in the observed slow response.

We are unaware of previous reports on this concentration dependent change in fragmentation pattern, although most of them calibrated over a small range of concentrations (Willis et al., 2016, Huang et al., 2017). It is worth noting that Huang et al. (2015) reports a value of 0.10±0.02 for f(CH$_3$SO$_2$), and their error bar does suggest variability on a similar scale as we found for unspecified reasons.
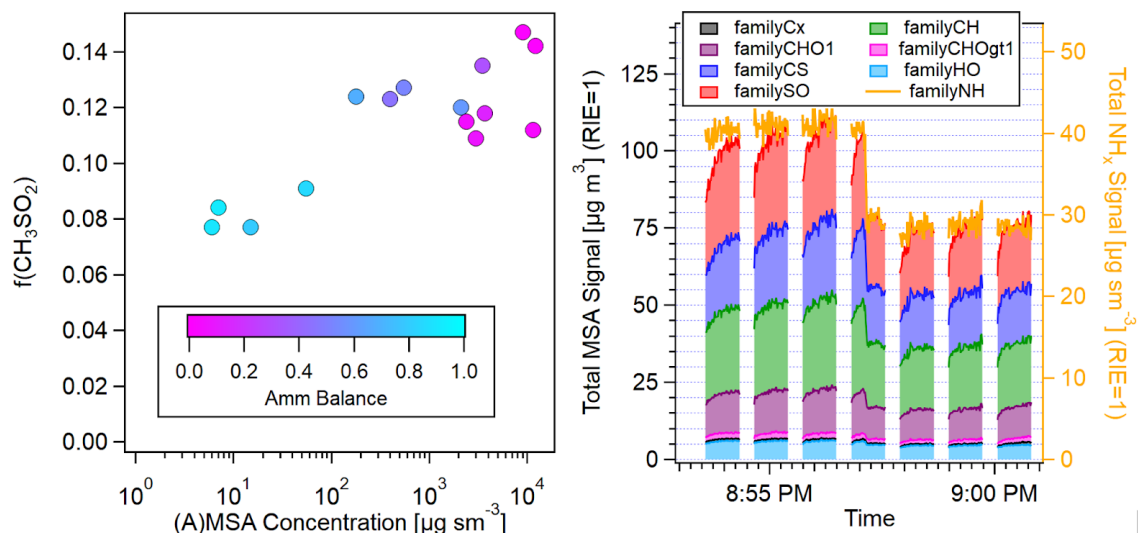
Figure S17. (left) Summary of all the marker ratios found in ATom calibrations as a function of MSA concentration, both using AMSA (excluding ammonium) and MSA. (right) Timeseries of the total ion signal (classified into AMS families) of MSA and NH_4 (both at RIE of 1) for a an AMSA calibration with 50 µg sm-3 of MSA, showing that for each acquisition cycle for some subset of the ions (mostly SO_x and CS) there is an equilibration time which depends on concentration and that is not observed for NH_4. This results in a time-dependent response that is especially pronounced at higher concentrations and hence affects both f(CH_3SO_2) and RIE_{MSA} (relative to RIE_{NH4}).

Since all the calibration with acidic MSA in our study were done at high concentrations, this could result in a potential uncertainty in the AMS fragmentation pattern of MSA (vs AMSA) and a potential bias in quantifying MSA in some of the highly acidic environments found in ATom. In order to further address this potential source of uncertainty for the ambient data, the data from the ATom-1 deployment was analyzed by positive matrix factorization (PMF) (Paatero 1994, Ulbrich et al., 2009) to extract a (calibration independent) MSA mass spectral profile. This was done by combining the organic and sulfate ions from the full mission at 1 min resolution (for improved fitting accuracy and detection limits, see Schroder et al., 2018) and performing PMF analysis with the PMF Evaluation Panel (PET) v3.01 (Ulbrich et al., 2009). Best results were achieved after downweighting the SO_x ions by 10x to make their weight in the weighted residual comparable to those of the larger organic ions. Figure S18a and b compares the spectra of the MSA factor obtained with the MS Spectra from the low concentration AMSA calibrations, showing excellent agreement for all ions except CH_3^+ (which is less specific than most other ions in the spectrum, since it can arise from a myriad of other OA species). Importantly, f(CH_3SO_2) in both cases is nearly identical (7.9% for the PMF factor vs 7.8% for the calibrations), confirming the validity of the low-concentration calibrations and also their applicability for ATom-1 (where no in-field calibrations for MSA were conducted).

Figure S18. (top) Comparison of the MSA Factor extracted from PMF analysis of the full sulfate+OA dataset during ATom-1 with the calibration spectrum of $NH_4SO_3CH_3$ (AMSA) taken at low concentrations, (a) on a linear scale and (b) on a logarithmic scale . (bottom) Scatter plot of the total signal for the $CH_3SO_2^+$ ion for the ATom-1 campaign vs. the MSA PMF Factor concentration (c) on a linear scale and (d) on a logarithmic scale as a function of acidity. The very highly correlated behavior independent of acidity suggests that for ambient data $f(CH_3SO_2)$ does not significantly change as a function of acidity.

However, the mass spectrum of the PMF Factor is a campaign average that is primarily weighted towards the often not-so-acidic marine boundary layer passes where the factor concentration was highest. To examine if MSA found under acidic conditions (mostly in the free troposphere) could have a different fragmentation pattern, it is instructive to look at the correlation of the $CH_3SO_2^+$ ion with the PMF factor. If pure MSA had a different $f(CH_3SO_2)$ than AMSA, this would lead to a deviation from the 7.9% slope line prescribed by PMF. However, despite the very high acidities that were

sometimes encountered while sampling MSA (pH<0), no significant deviation from linear behavior is observed over several orders of magnitude (Figure S18c and d). We hence conclude that there is no evidence for $f(CH_3SO_2)$ being a function of MSA acidity, and that even if the relative fractions of other ions were to change slightly as a function of acidity, quantification of MSA based on Eq. S1 should not be affected.

Hence, with a value of $f(CH_3SO_2)$ of 0.08±0.003 (average of low concentration calibrations and PMF factor), the combined inverse scaling factor of MSA relative to the CH_3SO_2 ion for ATom is 0.136±0.011, i.e. a combined multiplicative factor of 7.35 to translate $[CH_3SO_2^+]$ (in nitrate-equivalent concentration units; Jimenez et al., 2003) to [MSA] per Eq. S1 (referred in the following as the scaling factor, $S(CH_3SO_2)$).

$$S(CH_3SO_2) = \frac{1}{RIE(MSA) * f(CH_3SO_2)} \quad (Eq. S2)$$

S5.5 Comparison with previous studies

Table S4 summarizes all the studies where to the best of our knowledge both the marker fraction and the RIE for total MSA signal have been reported. It should be noted that only Willis et al. (2016) and Huang et al. (2017) directly measured RIE_{MSA}. In both cases, the mass closure method was used with reportedly pure, acidic MSA (although some neutralization was observed prior to analysis). While the linearity of their calibrations strongly suggests that doubly charged particles were not sampled, as noted above the shorter acquisition sequence might have resulted in a smaller RIE_{MSA} depending on the fraction of slower response in their instruments. In addition, evaporation and neutralization would still be a concern that could possibly lead to a potentially reduced RIE_{MSA}. Phinney et al. (2006) used RIE_{SO4}, while Schmale et al. (2013) used RIE_{OA} (consistent with their determination of MSA by PMF of OA, which also likely explains the low value of f(CH_3SO_2)). Both Huang et al. (2015) and Zorn et al (2008) used an averaged RIE of OA and sulfate (in Zorn's case an arithmetic average, in Huang's case a mass-weighted one).

While all reported values for RIE_{MSA} are lower than the one determined in this work, part of this difference may be due to instrument-to-instrument variability. It is worth noting that RIE_{SO4} in the CU AMS (determined by in-situ calibrations) is often significantly higher than the default RIE_{SO4} used by the other groups (1.5-1.7 vs 1.15-1.2) (Canagaratna et al., 2007), which might be due to a higher general sensitivity in this instrument for larger ions as well as the longer acquisition cycle compared to a regular AMS. However, this may not imply that RIE_{MSA} and RIE_{SO4} should be comparable for a given AMS. Sulfate mass in the AMS (based on the default fragmentation table, Allan et al., 2004) includes a large contribution of water (31%) and sulfur (7%) ions, significantly larger than what was found in this study for MSA (5% total).

Given the high variability in the determinations of $f(CH_3SO_2)$ it would be hence preferable to compare the scaling factor $S(CH_3SO_2)$ used to actually relate CH_3SO_2 to MSA (Table S4), but given that, as already discussed, most studies did not directly measure RIE_{MSA}, the variability of this parameter is also quite large. The fact that even in the cases where both RIE_{MSA} and $f(CH_3SO_2)$ were determined (Willis et al., 2016; Huang et al., 2017 and this work) the variability is $S(CH_3SO_2)$ is over a factor of 3 emphasizes

the instrumental variability and the need for careful calibrations of both RIE_{MSA} and $f(CH_3SO_2)$ in studies where MSA from AMS data is reported.

Table S4: RIE_{MSA}, as well as the relative abundance of the marker ion $f(CH_3SO_2)$ in previously reported calibrations of AMS response to MSA. Also listed is the effective scaling factor that results from these two quantities, $S(CH_3SO_2)$.

$f(CH_3SO_2)$, %	RIE_{MSA}	$S(CH_3SO_2)$	Reference
6.9	1.15	12.6	Phinney et al, 2006 (Q-AMS)
9	1.3	8.6	Zorn et al, 2008
4	1.4	17.9	Schmale et al, 2013 (PMF)
9.7	1.3	8	Huang et al, 2015
12.4	1.33	6.1	Willis et al, 2016
4	1.27	19.7	Huang et al, 2017
7.9	1.70 ± 0.08	7.4	This work

S5.6 Details of the Single Particle Calibrations, including CE of pure MSA

  Previous AMS studies on MSA have often assumed that due to acidity and phase, MSA should have a collection efficiency (CE, Middlebrook et al, 2012) of 1 (i.e. that pure particles do not bounce off the vaporizer), but this has not been confirmed previously. It is also not clear if the same applies for the semivolatile, yet non-acidic and solid at room temperature AMSA. Hence the CE of AMSA was determined using the single particle method (Canagaratna et al, 2007) using the Event Trigger acquisition mode of the AMS DAQ software.

  Both monodisperse 400 nm ammonium nitrate (AN in the following, Aldrich, >99%) and AMSA particles were introduced into the AMS and detected by triggering on m/z 30 and 46 (NO^+ and NO_2^+) for AN and m/z 15 and 79 for AMSA ($CH_3^+ + NH^+$ and $CH_3SO_2^+$) (Figure S19). For the fast evaporating AN, we found that the AMS detected 89% of the particles compared to a collocated CPC, consistent with the inlet transmission close to 100% efficient observed for this instrument (Schroder et al, 2018). For the AMSA particles that have a similar effective density (1.48 g cm^{-3} for AMSA vs 1.42 g cm^{-3} for AN) and hence should be transmitted at the same rate, we found a ratio of AMS single particle detection to CPC of 93%, hence confirming that for AMSA, CE~1.
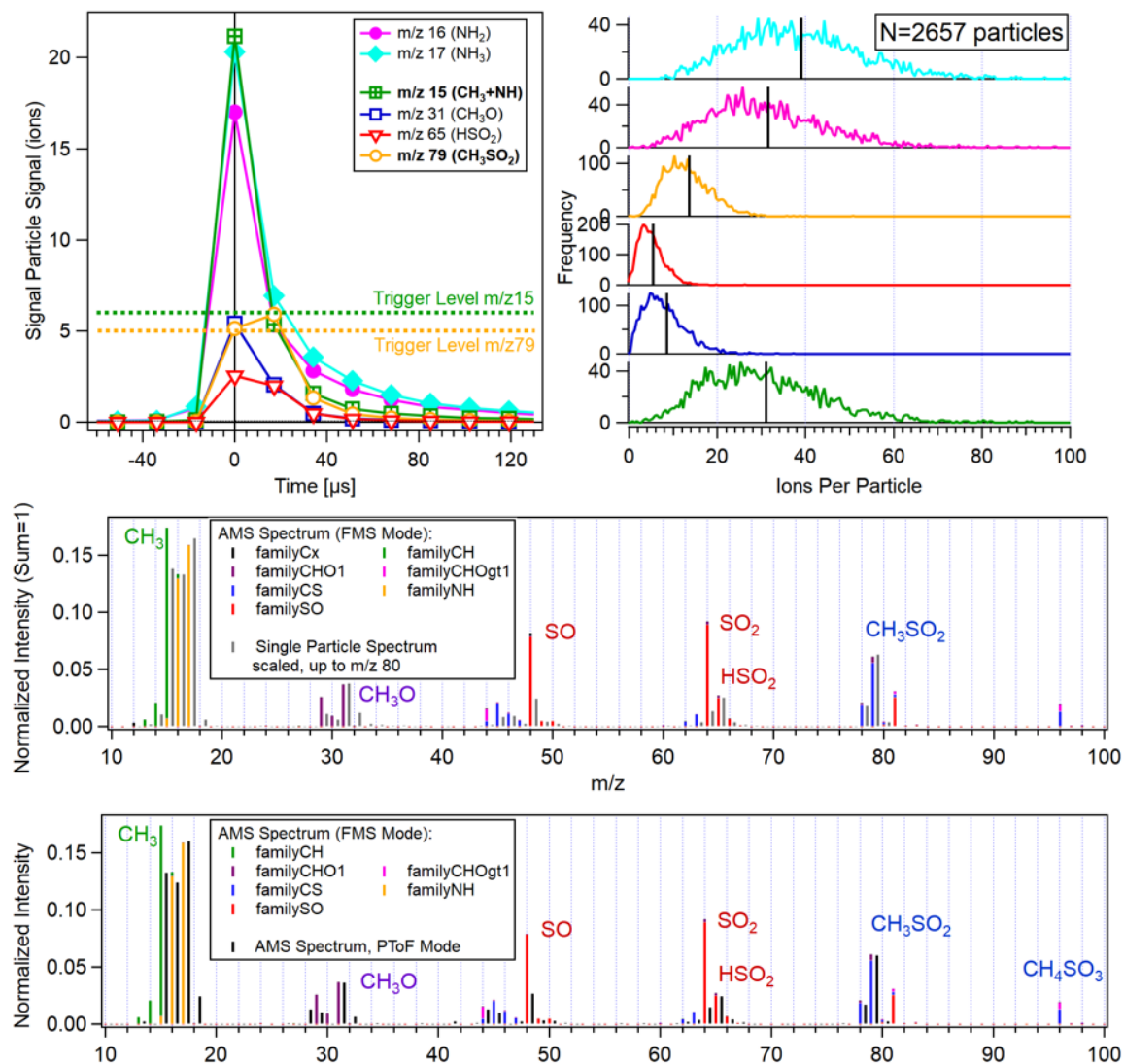
Figure S19. (top left) Average timetraces of the single particle signals at several mass to charge ratios for both the cation (NH_4) and anion (CH_3SO_3) recorded for 400 nm $NH_4CH_3SO_3$ particles being sampled into the AMS in ET mode. To trigger the single particle acquisition, either of the UMR m/z in bold (m/z 15 and 79) had to cross the prescribe threshold (dotted lines). (Right) Histograms of the total ions per particle recorded for each UMR m/z mass (2657 valid events). Black lines show the average values used in the IE calculations. (middle) Comparison of the immediate vaporization MS observed in the single particle experiments with the calibration spectrum taken in regular acquisition mode (FMS). (bottom) Comparison of the immediate vaporization MS observed in PToF mode with the calibration spectrum taken in FMS mode.

Despite the fast vaporization and detection of (nearly) every single particle, the MS spectrum recorded in single particle mode (Figure S19, 200 µs integration time) and ePToF mode (14 ms integration time) show significant differences when compared to the regular (ambient) MS mode (FMS, 1 s integration time, Kimmel et al, 2011). Most of the

SO_x^+ ions (and CH_3^+) have lower relative intensities at the shorter integration times, suggesting that these are released on longer timescales from the vaporizer. This different response times and hence, equilibration times for different components of the spectrum are likely also responsible for the spectral changes observed when varying the concentration of MSA over large ranges (Figure S16). For ambient data acquired during the ATom mission, this is clearly not a concern, as shown by the PMF analysis, but this effect could impact laboratory studies involving MSA and AMS detection via the marker method.

S5.7 ATom Data status

As detailed in the headers of the currently posted data (Wofsy et al., 2018), currently some fraction of the MSA mass is attributed to sulfate and some to OA. While these errors are typically small, future revisions will incorporate a correction to those species based on the quantification of MSA detailed above.

References

Allan, J. D., Delia, A. E., Coe, H., Bower, K. N., Alfarra, M. R. R., Jimenez, J. L., Middlebrook, A. M., Drewnick, F., Onasch, T. B., Canagaratna, M. R., Jayne, J. T. and Worsnop, D. R.: A generalised method for the extraction of chemically resolved mass spectra from Aerodyne aerosol mass spectrometer data, J. Aerosol Sci., 35(7), 909–922, doi:10.1016/j.jaerosci.2004.02.007, 2004.

Canagaratna, M. R., Jayne, J. T. J. T., Jimenez, J. L., Allan, J. D., Alfarra, M. R., Zhang, Q. Q., Onasch, T. B., Drewnick, F., Coe, H., Middlebrook, A. M., Delia, A., Williams, L. R., Trimborn, A. M., Northway, M. J., DeCarlo, P. F., Kolb, C. E., Davidovits, P. and Worsnop, D. R.: Chemical and microphysical characterization of ambient aerosols with the Aerodyne Aerosol Mass Spectrometer, Mass Spectrom. Rev., 26(2), 185–222, doi:10.1002/mas, 2007

Peter F. DeCarlo, Jay G. Slowik, Douglas R. Worsnop, Paul Davidovits & Jose L. Jimenez (2004) Particle Morphology and Density Characterization by Combined Mobility and Aerodynamic Diameter Measurements. Part 1: Theory, Aerosol Science and Technology, 38:12, 1185-1205, DOI: 10.1080/027868290903907

Guthrie, J.P.:Hydrolysis of esters of oxy acids: pKa values for strong acids; Brønsted relationship for attack of water at methyl; free energies of hydrolysis of esters of oxy acids; and a linear relationship between free energy of hydrolysis and pKa holding over a range of 20 pK units, Can. J. Chem., 56:2342-2354, 1978

Hu, W., Campuzano-Jost, P., Day, D. A., Croteau, P., Canagaratna, M. R., Jayne, J. T., Worsnop, D. R. and Jimenez, J. L.: Evaluation of the new capture vapourizer for aerosol mass spectrometers (AMS) through laboratory studies of inorganic species, Atmos. Meas. Tech., 10(6), 2897–2921, doi:10.5194/amt-10-2897-2017, 2017.

Huang, D. D., Li, Y. J., Lee, B.P and Chan, C. K.: Analysis of Organic Sulfur Compounds in Atmospheric Aerosols at the HKUST Supersite in Hong Kong Using HR-ToF-AMS. Environ. Sci. Tech. 49 (6), 3672-3679 2015

Huang, S., Poulain, L., van Pinxteren, D., van Pinxteren, M., Wu, Z., Herrmann, H. and Wiedensohler, A.: Latitudinal and Seasonal Distribution of Particulate MSA over the Atlantic using a Validated Quantification Method with HR-ToF-AMS, Environ. Sci. Technol., 51(1), 418–426, doi:10.1021/acs.est.6b03186, 2017.

Jimenez, J. L., Canagaratna, M. R., Drewnick, F., Allan, J. D., Alfarra, M. R., Middlebrook, A. M., Slowik, J. G., Zhang, Q., Coe, H., Jayne, J. T., Worsnop, D. R., Rami Alfarra, M., Middlebrook, A. M., Slowik, J. G., Zhang, Q., Coe, H., Jayne, J. T. and Worsnop, D. R.: Comment on "The effects of molecular weight and thermal decomposition on the sensitivity of a thermal desorption aerosol mass spectrometer," Aerosol Sci. Technol., 50(9), i–xv, doi:10.1080/02786826.2016.1205728, 2016.

Kimmel, J. R., Farmer, D. K., Cubison, M. J., Sueper, D., Tanner, C., Nemitz, E., Worsnop, D. R., Gonin, M. and Jimenez, J. L.: Real-time aerosol mass spectrometry with millisecond resolution, Int. J. Mass Spectrom., 303(1), 15–26, doi:10.1016/j.ijms.2010.12.004, 2011.

Lide, D.R. CRC Handbook of Chemistry and Physics 88TH Edition 2007-2008. CRC Press, Taylor & Francis, Boca Raton, FL 2007, p. 3-326

Middlebrook, A. M., Bahreini, R., Jimenez, J. L. and Canagaratna, M. R.: Evaluation of Composition-Dependent Collection Efficiencies for the Aerodyne Aerosol Mass Spectrometer using Field Data, Aerosol Sci. Technol., 46(3), 258–271, doi:10.1080/02786826.2011.620041, 2012.

Paatero, P. and Tapper, U.: Positive Matrix Factorization - A Nonnegative Factor Model With Optimal Utilization of Error-Estimates of Data Values, Environmetrics, 5(2), 111–126, 1994.

Phinney, L., Richard Leaitch, W., Lohmann, U., Boudries, H., Worsnop, D. R., Jayne, J. T., Toom-Sauntry, D., Wadleigh, M., Sharma, S., Shantz, N., Leaitch, W. R., Lohmann, U., Boudries, H., Worsnop, D. R., Jayne, J. T., Toom-Sauntry, D., Wadleigh, M., Sharma, S., Shantz, N., Richard Leaitch, W., Lohmann, U., Boudries, H., Worsnop, D. R., Jayne, J. T., Toom-Sauntry, D., Wadleigh, M., Sharma, S., Shantz, N., Leaitch, W. R., Lohmann, U., Boudries, H., Worsnop, D. R., Jayne, J. T., Toom-Sauntry, D., Wadleigh, M., Sharma, S. and Shantz, N.: Characterization of the aerosol over the sub-arctic north east Pacific Ocean, Deep. Res. II-Topical Stud. Oceanogr., 53(20–22), 2410–2433, doi:10.1016/j.dsr2.2006.05.044|ISSN 0967-0645, 2006.

Schmale, J., Schneider, J., Nemitz, E., Tang, Y. S., Dragosits, U., Blackall, T. D., Trathan, P. N., Phillips, G. J., Sutton, M. and Braban, C. F.: Sub-Antarctic marine aerosol: dominant contributions from biogenic sources, Atmos. Chem. Phys., 13(17), 8669–8694, doi:10.5194/acp-13-8669-2013, 2013.

Schroder, J. C., Campuzano-Jost, P., Day, D. A., Shah, V., Larson, K., Sommers, J. M., Sullivan, A. P. Campos, T. Reeves, J. M. Hills, A., Hornbrook, R. S., Blake, N. J., Scheuer, E., Guo, H., Fibiger, D. L. McDuffie, E. E., Hayes, P. L., Weber, R. J., Dibb, J. E. Apel, E. C., Jaeglé, L. Brown, S. S. Thornton, J. A. and Jimenez, J. L. Sources and secondary production of organic aerosols in the northeastern United States during WINTER. Journal of Geophysical Research: Atmospheres, 123, 7771–7796. 2018

Tang, I. N. and Munkelwitz, H. R.: Determination of Vapor Pressure from Droplet Evaporation Kinetics, Journal of Colloid and Interface Science, 141, (1), 1991

Ulbrich, I. M., Canagaratna, M. R., Zhang, Q., Worsnop, D. R. and Jimenez, J. L.: Interpretation of organic components from Positive Matrix Factorization of aerosol mass spectrometric data, Atmos. Chem. Phys., 9(9), 2891–2918, doi:10.5194/acp-9-2891-2009, 2009.

Willis, M. D., Burkart, J., Thomas, J. L., Köllner, F., Schneider, J., Bozem, H., Hoor, P. M., Aliabadi, A. A., Schulz, H., Herber, A. B., Leaitch, W. R. and Abbatt, J. P. D.: Growth of nucleation mode particles in the summertime Arctic: a case study, Atmos. Chem. Phys., 16(12), 7663–7679, doi:10.5194/acp-16-7663-2016, 2016.

Wofsy, S.C., S. Afshar, H.M. Allen, E. Apel, E.C. Asher, B. Barletta, J. Bent, H. Bian, B.C. Biggs, D.R. Blake, N. Blake, I. Bourgeois, C.A. Brock, W.H. Brune, J.W. Budney, T.P. Bui, A. Butler, P. Campuzano-Jost, C.S. Chang, M. Chin, R. Commane, G. Correa, J.D. Crounse, P. D. Cullis, B.C. Daube, D.A. Day, J.M. Dean-Day, J.E. Dibb, J.P. DiGangi, G.S. Diskin, M. Dollner, J.W. Elkins, F. Erdesz, A.M. Fiore, C.M. Flynn, K. Froyd, D.W. Gesler, S.R. Hall, T.F. Hanisco, R.A. Hannun, A.J. Hills, E.J. Hintsa, A. Hoffman, R.S. Hornbrook, L.G. Huey, S. Hughes, J.L. Jimenez, B.J. Johnson, J.M. Katich, R. Keeling, M.J. Kim, A. Kupc, L.R. Lait, J.-F. Lamarque, J. Liu, K. McKain, R.J. Mclaughlin, S. Meinardi, D.O. Miller, S.A. Montzka, F.L. Moore, E.J. Morgan, D.M. Murphy, L.T. Murray, B.A. Nault, J.A. Neuman, P.A. Newman, J.M. Nicely, X. Pan, W. Paplawsky, J. Peischl, M.J. Prather, D.J. Price, E. Ray, J.M. Reeves, M. Richardson, A.W. Rollins, K.H. Rosenlof, T.B. Ryerson, E. Scheuer, G.P. Schill, J.C. Schroder, J.P. Schwarz, J.M. St.Clair, S.D. Steenrod, B.B. Stephens, S.A. Strode, C. Sweeney, D. Tanner, A.P. Teng, A.B. Thames, C.R. Thompson, K. Ullmann, P.R. Veres, N. Vieznor, N.L. Wagner, A. Watt, R. Weber, B. Weinzierl, P. Wennberg, C.J. Williamson, J.C. Wilson, G.M. Wolfe, C.T. Woods, and L.H. Zeng. 2018. ATom: Merged Atmospheric Chemistry, Trace Gases, and Aerosols. ORNL DAAC, Oak Ridge, Tennessee, USA. https://doi.org/10.3334/ORNLDAAC/1581

Zorn, S. R., Drewnick, F., Schott, M., Hoffmann, T. and Borrmann, S.: Characterization of the South Atlantic marine boundary layer aerosol using an aerodyne aerosol mass spectrometer, Atmos. Chem. Phys., 8(16), 4711–4728, doi:10.5194/acp-8-4711-2008, 2008.